universe

MDPI

Review

Solar Radio Emissions and Ultralight Dark Matter

Haipeng An [1,2,3,4], Shuailiang Ge [3,5,*] and Jia Liu [3,5]

[1] Department of Physics, Tsinghua University, Beijing 100084, China
[2] Center for High Energy Physics, Tsinghua University, Beijing 100084, China
[3] Center for High Energy Physics, Peking University, Beijing 100871, China
[4] Frontier Science Center for Quantum Information, Beijing 100084, China
[5] State Key Laboratory of Nuclear Physics and Technology, School of Physics, Peking University, Beijing 100871, China
* Correspondence: sge@pku.edu.cn

Abstract: Ultralight axions and dark photons are well-motivated dark matter candidates. Inside the plasma, once the mass of ultralight dark matter candidates equals the plasma frequency, they can resonantly convert into electromagnetic waves, due to the coupling between the ultralight dark matter particles and the standard model photons. The converted electromagnetic waves are monochromatic. In this article, we review the development of using radio detectors to search for ultralight dark matter conversions in the solar corona and solar wind plasma.

Keywords: solar radio emissions; ultralight dark matter; dark photon; axion; resonant conversion

check for updates

Citation: An, H.; Ge, S.; Liu, J. Solar Radio Emissions and Ultralight Dark Matter. *Universe* **2023**, *9*, 142. https://doi.org/10.3390/universe9030142

Academic Editors: Jing Huang and Baolin Tan

Received: 15 January 2023
Revised: 1 March 2023
Accepted: 3 March 2023
Published: 7 March 2023

1. Introduction

There is overwhelming evidence from astronomical and cosmological observations supporting that about one-fourth of the energy density in today's universe is composed of dark matter. However, the particle nature of dark matter is still mysterious. Because of the null results of searching for WIMPs [1–3], more and more attention has been attracted to ultralight dark matter candidates such as the QCD axion [4], axion-like particles [5], and dark photons [6–9]. Originally, the theory of the QCD axion was put forward to resolve the strong CP problem via the known Peccei–Quinn mechanism [10–13]. Soon after this, it was shown that, as a bonus, QCD axions are suitable dark matter candidates [4]. In addition, many models such as the string theory give rise to axion-like particles which have similar features as QCD axions in coupling with the standard model of particle physics. Similarly, axion-like particles can also serve as dark matter candidates. In the rest of the paper, we will call both the QCD axion and axion-like particles axions. There are multiple ways in the early Universe of generating axions: both the misalignment mechanism [14–16] and the decay of axionic topological defects such as domain walls and strings [17,18] can produce an appropriate amount of axions as dark matter. On the other hand, a dark photon is usually a $U(1)$ gauge boson which kinetically mixes with the standard model photons with a tiny coupling strength [19–24]. Dark photons are also good dark matter candidates [6–9] and can be generated in multiple ways, such as parametric resonances [25–30], inflationary fluctuations [9,31–40], the misalignment mechanism [7,8,41–43], and cosmic string decay [44]. Current measurements show that the local dark matter density in the solar system, $\rho_{\rm DM}$, is about 0.3 GeV/cm^3 [45,46]. In this paper, we assume that the dark matter is saturated either by axions or dark photons.

The interaction between axions and electromagnetic fields makes it possible for the axion dark matter to convert to electromagnetic waves in a magnetic field. If plasma exists, the interaction between the electromagnetic field and charged particles in the plasma can induce an effective mass for transverse photons, which equals the plasma frequency ω_p. Thus, in the region that $\omega_p = m_{\rm DM}$, the axion DM will resonantly convert to electromagnetic waves. For dark photon dark matter, the plasma will also regenerate the mixing of the

dark photon field and the photon field. Thus, the once diagonalized fields can convert to each other again inside the plasma. Therefore the dark photon dark matter can also convert into electromagnetic waves in the region $\omega_p = m_{\rm DM}$. The energy of the converted photon equals the energy of the dark matter particle, which can be written as $m_{\rm DM} + E_{k\rm DM}$, where $E_{k\rm DM}$ is the kinetic energy of each dark matter particle. In the galactic halo, we have $E_{k\rm DM} \sim 10^{-6} m_{\rm DM}$. Thus, we expect a monochromatic electromagnetic wave signal produced by ultralight dark matter conversions. To take advantage of the resonant conversion to search for ultralight dark matter, we need to first find a large plasma. Secondly, the region between the conversion region and the detector must be transparent for the converted electromagnetic wave to propagate to the detector. A perfect plasma that we can use is the Sun's corona. The distribution of temperature and plasma density in the Sun's corona is shown in Figure 1a, where one can calculate that ω_p ranges from about 10^{-6} to 10^{-7} eV. Thus, if the mass of axion dark matter or dark photon dark matter falls in this region, it can produce monochromatic electromagnetic wave signals. The frequency in this region is about 10–1 GHz, which is in the radio wave band. There is already a lot of radio observation apparatus toward the Sun, such as the low-frequency array (LOFAR) [47], having collected plenty of solar radio data, which we can search for ultralight dark matter conversion signals. There will also be future projects, such as the square kilometre array (SKA) [48] and the upgraded five hundred metre aperture spherical radio telescope (FAST), which may provide more precise solar data in the future.

The earth's ionosphere also provides the plasma for the ultralight dark matter conversion. However, the frequency range is about 4–6 MHz, which is polluted by human activities, and therefore cannot be used to search for ultralight dark matter. Furthermore, because of the screening effect of the earth's ionosphere, there are no terrestrial radio telescopes with frequency ranges below 10 MHz. Thus, if the frequency of the ultralight dark matter ($m_{\rm DM}/(2\pi)$) is smaller than 10 MHz, we need to go outer space to search for the conversion signal. The reason the conversion can still happen is that solar wind provides charged particles in the inter-region between the Sun and the Earth. In Figure 1b, one can see that ω_p in the region between the Sun and the Earth is all the way down to 10^{-10} eV. Solar probe satellites with long-wave radio spectrometers, such as the STEREO satellites [49] and the Parker solar probe [50], have been sent out to observe solar activities, and have collected a lot of data. Thus, one can search for the conversion signal in these observation data.

Similar ideas have been proposed to search for radio waves from axion resonant conversion in the mega magnetic field around neutron stars [51–53] and white dwarfs [54–57]. On the other hand, solar radio emissions are also related to other dark matter models. For instance, the impulse radio events observed by the Murchison widefield array (MWA) [58] may be explained by the annihilation of axion–quark–nugget dark matter [59–63] in the solar corona, the energy released from which may account for the solar corona heating mystery [64–66].

In this article, we review the recent developments in searching for ultralight dark matter in solar radio observations. In Section 2, we review particle physics models for axions and dark photons, focusing on their interactions with electromagnetic waves. In Section 3, we present the calculation of the conversion probabilities for axions and dark photons. In Section 4, we review the calculation of the propagation of the converted electromagnetic waves. We discuss the sensitivities of the radio telescopes for such resonant signals in Section 5. We summarize the results in Section 6.

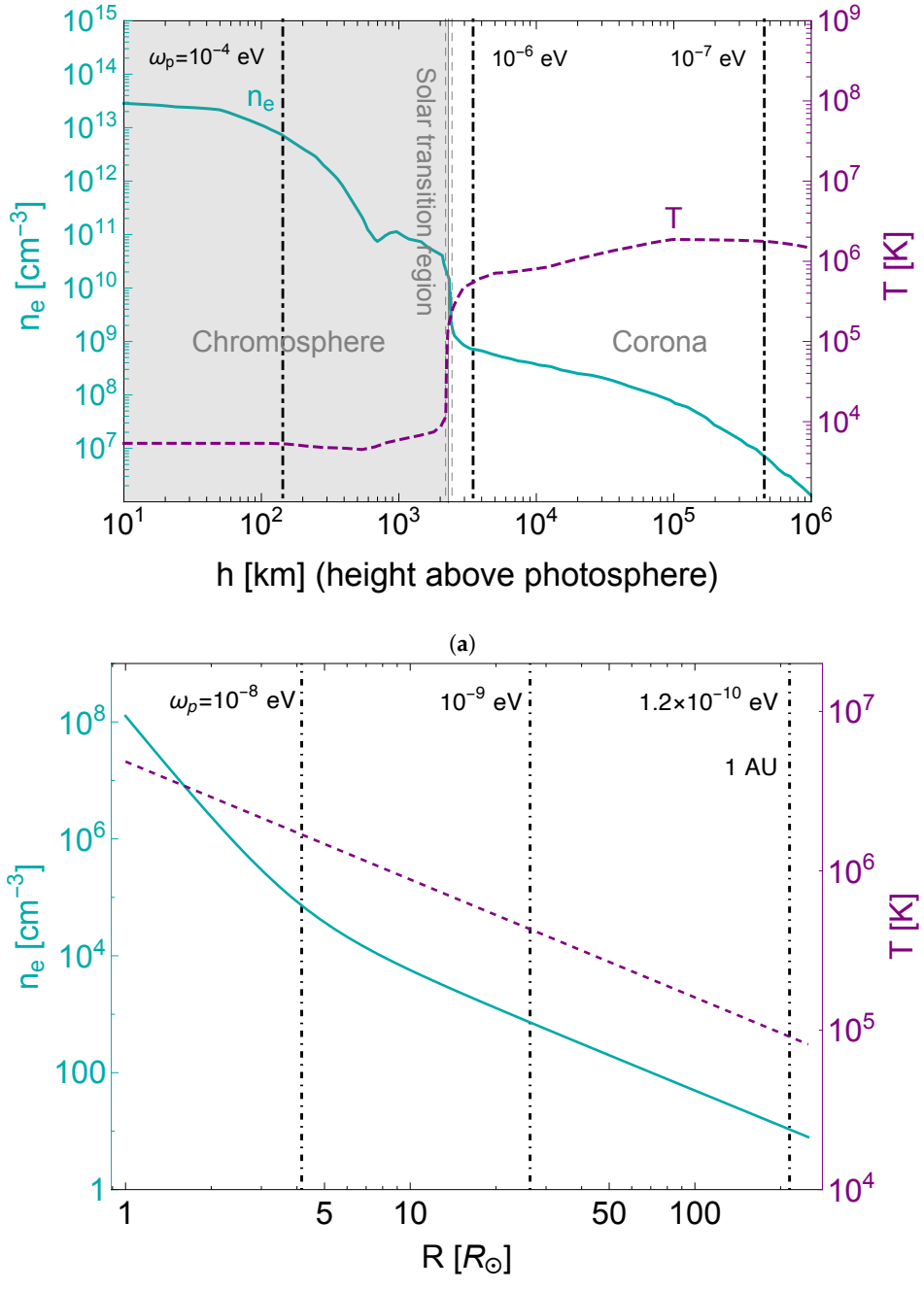

Figure 1. (**a**) Quiet-Sun electron density n_e and temperature T profiles in the solar atmosphere above the photosphere. Figure adapted from [67] based on the result of [68]. (**b**) n_e and T (thermal temperature of electrons) profiles in the solar-wind plasma with the distance extending up to about 1 AU. The n_e profile is based on the in situ measurements of the Parker solar probe [69] and then fitted by the relation $n_e(r) \sim \left[3.3\times10^5(r/R_\odot)^{-2} + 4.1\times10^6(r/R_\odot)^{-4} + 8.0\times10^7(r/R_\odot)^{-6}\right]$ cm^{-3} given in [70]. The T profile is the relation $T(r) \sim 418$ eV $\times (r/R_\odot)^{-0.74}$ [69] based on the in situ measurements.

2. Ultralight Dark Matter

An axion is a pseudoscalar particle whose interaction with the electromagnetic part can be written as

$$\mathcal{L}_{\rm axion} = -\frac{1}{4}F^{\mu\nu}F_{\mu\nu} + \frac{1}{2}\partial_\mu a \partial^\mu a - \frac{1}{2}m_a^2 a^2 + \frac{1}{4}a g_{a\gamma\gamma}F^{\mu\nu}\tilde{F}_{\mu\nu}. \quad (1)$$

where a is the axion field and m_a is its mass. $F^{\mu\nu} = \partial^\mu A^\nu - \partial^\nu A^\mu$ is the field strength of the standard model photon and $\tilde{F}_{\mu\nu} = \varepsilon_{\mu\nu\alpha\beta}/2 \cdot F^{\alpha\beta}$ is the dual field strength. $g_{a\gamma\gamma}$ is the coupling between the axion and the standard model photon. The interaction term in Equation (1) can be further simplified to $-g_{a\gamma\gamma} a \mathbf{E} \cdot \mathbf{B}$ in terms of the electric and magnetic fields.

A dark photon is a $U(1)$ gauge boson that, after electroweak symmetry breaking, interacts with the standard model photon via the following Lagrangian:

$$\mathcal{L}_{dp} = -\frac{1}{4} F^{\mu\nu} F_{\mu\nu} - \frac{1}{4} F'^{\mu\nu} F'_{\mu\nu} + \frac{1}{2} m_{A'}^2 A'^2 - \frac{\epsilon}{2} F'^{\mu\nu} F_{\mu\nu}. \tag{2}$$

where $F'^{\mu\nu} = \partial^\mu A'^\nu - \partial^\nu A'^\mu$ is the field strength of dark photon and $m_{A'}$ is its mass. ϵ is the kinetic mixing strength between the dark photon and the photon. To more conveniently study the conversion between a dark photon and a photon, we can diagonalize Equation (2) in the interaction basis with the following field redefinition:

$$\begin{pmatrix} A \\ A' \end{pmatrix} \to \begin{pmatrix} \frac{1}{\sqrt{1-\epsilon^2}} & 0 \\ \frac{-\epsilon}{\sqrt{1-\epsilon^2}} & 1 \end{pmatrix} \begin{pmatrix} A \\ A' \end{pmatrix}, \tag{3}$$

and Equation (2) becomes

$$\mathcal{L}_{dp} = -\frac{1}{4} F^{\mu\nu} F_{\mu\nu} - \frac{1}{4} F'^{\mu\nu} F'_{\mu\nu} + \frac{1}{2} m_{A'}^2 A'^2 - \epsilon m_{A'}^2 A'_\mu A^\mu. \tag{4}$$

In solar plasma, photons will acquire an effective mass equal to the plasma frequency, $m_A = \omega_p$. The plasma is charge neutral consisting of electrons and ions. Ignoring the contributions of ions due to their large masses, we only care about the plasma frequency of electrons, which in the non-relativistic case is

$$\omega_p = \sqrt{\frac{4\pi\alpha n_e}{m_e}}. \tag{5}$$

where α is the fine structure constant, m_e is the electron mass, and n_e is the electron density. Therefore, for photons in plasma, we should add an effective mass term $\mathcal{L} \supset 1/2 \cdot \omega_p^2 A^2$ in the Lagrangians (1) and (4).

3. Conversion in Solar Plasma

The equations of motions corresponding to the Lagrangians (1) and (4) for the axion and dark photon cases can both be written in the form [71]

$$\left(\frac{\partial^2}{\partial t^2} - \frac{\partial^2}{\partial r^2} + \tilde{M} \right) \begin{pmatrix} A \\ X \end{pmatrix} = 0, \quad \tilde{M} = \begin{pmatrix} \tilde{\Delta}_{AA} & \tilde{\Delta}_{AX} \\ \tilde{\Delta}_{AX} & \tilde{\Delta}_{XX} \end{pmatrix}. \tag{6}$$

where X denotes either axion a or dark photon A'. For the axion case, we have

$$\tilde{\Delta}_{AA} = m_A^2 = \omega_p^2, \quad \tilde{\Delta}_{XX} = m_a^2, \quad \tilde{\Delta}_{AX} = -g_{a\gamma\gamma} |\boldsymbol{B}_T| \cdot \omega, \tag{7}$$

and for the dark photon case, we have

$$\tilde{\Delta}_{AA} = m_A^2 = \omega_p^2, \quad \tilde{\Delta}_{XX} = m_{A'}^2, \quad \tilde{\Delta}_{AX} = -\epsilon m_{A'}^2. \tag{8}$$

Since the external environment in the solar plasma mostly depends on the radial direction r (this is true for the dominant term Δ_{AA} which is determined by electron density according to Equation (5)), we only keep the spatial derivative in the radial direction in the equation of motion (Equation (6)) while ignoring trivial dynamics in the other two spatial dimensions.

Some differences between the axion case and the dark photon case are as follows. In comparison with the dark photon case, the conversion between axions and photons requires

the presence of a magnetic field $\boldsymbol{B}_T$ transverse to the axion trajectory. The solar magnetic field provides the source of $\boldsymbol{B}_T$. Due to the pseudoscalar feature of axions, the converted photons A in Equation (6) is polarized in the direction of $\boldsymbol{B}_T$ [56,71]. For the dark photon case, Equation (6) describes converted photons in two transverse modes perpendicular to the propagation trajectory.

We assume the solutions to the equation of motion (Equation (6)) are in the wave form:

$$A(t,r) = \tilde{A}(r)\exp(-i\omega t + ik_r r), \quad X(t,r) = \tilde{X}(r)\exp(-i\omega t + ik_r r) \tag{9}$$

where ω is the energy of the wave, $k = \sqrt{\omega^2 - m_X^2}$ is the momentum, and k_r is the momentum component in the radial direction. For resonant conversion to happen, we should have $m_A = m_X$ such that both ω and k of A and X match before and after the conversion. In the case we consider here where the dark matter velocity is non-relativistic $v \sim 10^{-3}c$, we have $\omega \simeq m_X$. Then, near the resonant layer in solar plasma, we have the following relation [71]:

$$\begin{aligned}\frac{\partial^2}{\partial t^2} - \frac{\partial^2}{\partial r^2} &= -\omega^2 - \frac{\partial^2}{\partial r^2} = -\left(k_r + i\frac{\partial}{\partial r}\right)\left(k_r - i\frac{\partial}{\partial r}\right) - m_X^2 - k_T^2 \\ &\simeq -2k_r\left(k_r + i\frac{\partial}{\partial r}\right) - m_X^2 - k_T^2.\end{aligned} \tag{10}$$

The last approximated relation holds because the parameters of solar plasma, e.g., plasma frequency, vary slowly in a length scale much larger than the wavelength $1/k_r$ such that

$$\left|\frac{\partial}{\partial r}\tilde{A}(r)\right| \ll k_r|\tilde{A}(r)|, \quad \left|\frac{\partial^2}{\partial r^2}\tilde{A}(r)\right| \ll k_r\left|\frac{\partial}{\partial r}\tilde{A}(r)\right|. \tag{11}$$

Therefore, using the relation in Equation (10), the equation of motion (Equation (6)) can be simplified to

$$\left(i\frac{\partial}{\partial r} - M\right)\begin{pmatrix}\tilde{A}(r)\\ \tilde{X}(r)\end{pmatrix} = 0 \tag{12}$$

where

$$\begin{aligned}&M = \frac{1}{2k_r}(\tilde{M} - m_X^2) \equiv M_0 + M_1, \\ &M_0 = \begin{pmatrix}\frac{1}{2k_r}(\omega_p^2 - m_X^2 - k_T^2) & 0\\ 0 & -\frac{1}{2k_r}k_T^2\end{pmatrix}, \quad M_1 = \begin{pmatrix}0 & \Delta_{AX}\\ \Delta_{AX} & 0\end{pmatrix}, \quad \Delta_{AX} \equiv \frac{\tilde{\Delta}_{AX}}{2k_r}.\end{aligned} \tag{13}$$

The off-diagonal matrix M_1 is suppressed by the coupling constant, either ϵ or $g_{a\gamma\gamma}$, and thus can be treated as a perturbative term. If we start with a X particle, $(A, X) = (0, 1)$ initially, then solving the equation of motion (Equation (12)) to the first order of M_1, the probability that X eventually converts to a photon A, namely, $(A, X) = (1, 0)$, is

$$P_{X\to\gamma} = \left|\int_{r_0}^{r} dr'\Delta_{AX}(r')\exp\left\{i\int_{r_0}^{r'} dr''\frac{1}{2k_r}\left[\omega_p^2(r'') - m_X^2\right]\right\}\right|^2. \tag{14}$$

We can solve the integration using the saddle-point method

$$\left|\int dr'\, g(r')\mathrm{e}^{-ih(r')}\right| \approx g(r_c)\sqrt{\frac{2\pi}{|h''(r_c)|}}, \quad h(r') \equiv \int_{r_0}^{r'} dr''\frac{1}{2k_r}\left[\omega_p^2(r'') - m_X^2\right] \tag{15}$$

where we have used the expression of norm to remove the redundant phase factor. r_c is the position when $h(r)$ reaches its local maximum/minimum $h'(r_c) = 0$, that is, the

position of resonant X-A conversion when $\omega_p(r_c) = m_X$. Only the second derivative plays an important role, the expression of which is

$$h''(r_c) = \frac{\omega_p}{k_r} \frac{\partial \omega_p(r)}{\partial r}\bigg|_{r=r_c}. \tag{16}$$

The length of the resonant layer δr_c can be estimated as the length that makes $h(r) \approx h(r_c) + 1/2 \cdot (r - r_c)^2 h''(r_c)$ change by 2π, so we obtain

$$\delta r_c \sim \sqrt{\frac{4\pi}{|h''(r_c)|}} \sim \sqrt{\frac{r_c v_r}{\omega_p}}. \tag{17}$$

The resonant layer is very thin, $\delta r_c / r_c \sim 10^{-6}$, for the typical values $r_c = R_\odot$, $\omega_p = 2\pi \cdot 100$ MHz, and $v_r = 10^{-3}c$.

Applying the saddle-point approximation as shown is Equation (15), we solve Equation (14) and obtain

$$P_{X\to\gamma} = \Delta_{AX}^2(r_c) \cdot \frac{2\pi k_r}{\omega_p} \left|\frac{\partial \omega_p}{\partial r}\right|^{-1}_{r=r_c}. \tag{18}$$

Then, for each case we have

$$P_{a\to\gamma} = \pi \frac{g_{a\gamma\gamma}^2 |\boldsymbol{B}_T|^2}{m_a} \frac{1}{v_r(r_c)} \left|\frac{\partial \ln \omega_p^2}{\partial r}\right|^{-1}_{r=r_c}, \quad \text{(axion case)} \tag{19}$$

and

$$P_{A'\to\gamma} \simeq \frac{2}{3} \pi \epsilon^2 m_{A'} \frac{1}{v_r(r_c)} \left|\frac{\partial \ln \omega_p^2}{\partial r}\right|^{-1}_{r=r_c}, \quad \text{(dark photon case)}. \tag{20}$$

Note that we have an extra prefactor $2/3$ in the dark photon case. This is because the converted photons polarize in three directions with equal probability but the longitudinal mode cannot propagate out of the plasma. In comparison, the photons converted from axions polarize only in one transverse mode parallel to $\boldsymbol{B}_T$ as mentioned above. Furthermore, the conversion probabilities for the two cases are related via the following replacement

$$\sqrt{\frac{2}{3}} \epsilon m_{A'}^2 \Leftrightarrow g_{a\gamma\gamma} |\boldsymbol{B}_T| \omega, \quad (\omega \simeq m_a, \text{non-relativistic}). \tag{21}$$

This relation is useful when we know the conversion rate of one case and directly calculate that of the other case.

4. Propagation of the Converted Photons

After the radio photons are converted from axions or dark photons, they will be refracted, absorbed, and scattered by thermal electrons in the plasma. We discuss these effects during the photon propagation in the following.

Refraction effect—The behaviour of converted photons propagating in the solar plasma obeys the rule of refraction:

$$\frac{n(r_c)}{n(r)} = \frac{\sin\theta(r)}{\sin\theta(r_c)}. \tag{22}$$

where $\theta(r)$ is the angle of incidence or refraction with respect to the radial direction. $n(r)$ is the refraction index as a function of distance, which is equal to the inverse of phase velocity:

$$n(r) = \frac{k}{\omega} = \sqrt{1 - \frac{\omega_p^2(r)}{\omega^2}}. \tag{23}$$

At the position of resonant conversion, $n(r_c) \simeq vs. \sim 10^{-3}$. Once the converted photons leave the resonant layer, the refraction index $n(r)$ quickly increases to values close to 1 as the number density of electrons n_e (and thus the plasma frequency, according to Equation (5)) abruptly decreases with the distance. For example, as we can see from Figure 1a, n_e drops by about two orders of magnitude from the height 10^4 km to the height 10^6 km. Therefore, the converted photons will quickly propagate nearly radially $\theta \simeq \pi/2$ after travelling a distance based on the refraction law (Equation (22)).

Absorption effect—In addition to the refraction effect discussed above, the converted photons could be absorbed by interacting with the plasma along the propagation. The absorption effect is mainly due to the inverse bremsstrahlung process, the rate of which is estimated as [67,72]

$$\Gamma_{\rm invB} \simeq \frac{8\pi\alpha^3 n_e n_I}{3m_e^2\omega^3}\sqrt{\frac{2\pi m_e}{T}}\ln\left(\frac{2T^2}{\omega_p^2}\right)\left(1-{\rm e}^{-\omega/T}\right). \tag{24}$$

where n_I is the number density of ions in the plasma. This equation is derived under the condition $\omega \ll T \ll m_e$, which is satisfied in both the solar corona and solar wind plasma, as can be seen in Figure 1. Taking into consideration the long-range Coulomb force cut off by the plasma screening effect (Debye screening length $\lambda_d \sim \sqrt{T/(m_e\omega_p^2)}$), we have the ln factor in Equation (24). At first glance, it seems that the inverse bremsstrahlung rate $\sim \omega^{-3}$ will diverge for low-energy photons, but the numerator factor $n_e n_I \simeq n_e^2 \propto \omega_p^4 \propto \omega^4$ at the resonant layer actually makes $\Gamma_{\rm invB}$ decease quickly as $\omega \to 0$.

Scattering effect—The converted photons also interact with plasma via Compton scattering, the rate of which is

$$\Gamma_{\rm Com} = \frac{8\pi\alpha^2}{3m_e^2}n_e. \tag{25}$$

Such interactions can shift the photon energy and propagation direction. We will elaborate more on this effect in the following.

To estimate how the converted photons are affected by the effects of absorption and scattering, one can define an attenuation factor by simply adding the two effects together, $\Gamma_{\rm att} = \Gamma_{\rm invB} + \Gamma_{\rm Com}$ [67]. Then, the survival probability of photons after conversion can be estimated as [67]

$$P_{\rm sur} \simeq \exp\left(-\int_{r_c}^{\infty}[\Gamma_{\rm att}(r)]/v_r dr\right). \tag{26}$$

It denotes the probability that a converted photon is neither absorbed nor scattered during propagation.

Compared with the inverse bremsstrahlung process (Equation (24)), the Compton scattering plays a minor role. This can be seen by taking the ratio of Equation (25) to Equation (24) which gives $\sim(m_e/T)^{-3/2} \ll 1$. In addition, the propagating photons can scatter with random electron density fluctuations (e.g., [73]), which is labelled as 'irregular refractions' in [74]. Ref. [73] treated the density fluctuations as effectively static, and therefore the scatterings do not change the photon energy but only the photon propagating direction.

Therefore, Equation (26) represents a simplified and conservative scenario. More realistically, the converted photons will be scattered in different directions with angular distribution. As pointed out in [73], the directions of solar radio emissions will be quickly randomized by the scattering effect (mainly due to electron density fluctuations) near the resonant region where the plasma frequency is equal to the emission frequency, while the large-scale refraction generally tends to shift the propagation path towards the radial direction. Solving exactly the evolution dominated by repeated scatterings and inverse bremsstrahlung processes is difficult, and this problem is usually transformed into the framework of Fokker–Planck Equation (e.g., [73,75–77]). Essentially, the Fokker–Planck equation can describe the evolution of the phase–space distribution $N(\boldsymbol{r}, \boldsymbol{k}, t)$ of photons,

where the refraction effect represented by the gradually varying $n_e(r)$, the absorption effect represented by a collision absorption coefficient, and the scattering effect represented by a diffusion tensor, are included [73,75]. Based on the Fokker–Planck equation, ref. [73] developed a numerical Monte Carlo ray-tracing method to study the three-dimensional stochastic propagation process of radio emissions where the anisotropic n_e fluctuation has been considered.

Applying the ray-tracing numerical code [73], ref. [78] studied the propagation of converted photons in the plasma. The survival probability $P_{\rm sur}$ defined in the numerical study is only related to absorption regardless of whether scattered or not, which is different from that in Equation (26). The scattering effect against the refraction effect is represented by the angular distribution function $g(\theta)$ where θ is the angle between the final propagation direction and the radial direction on the last scattering surface ($\sim 6R_\odot$, beyond which the interactions of photons with the plasma are negligible). The numerical results show that $P_{\rm sur} \simeq 0.5$–0.07 and $g(\theta)$ distributes mostly within the range $\theta \sim 0.15$ rad, in the radio frequency range 30–80 MHz, and both the two effects are stronger for higher frequencies.

5. Detection

For dark matter particles with typical initial velocity $v_0 \simeq 220$ km/s, the solar gravitational effect cannot be neglected when they travel close to the Sun since $GM_\odot/(R_\odot v_0^2) \simeq 3.45$ is an $\mathcal{O}(1)$ number. The trajectory of a dark matter particle from far away is hyperbolic in the solar gravitational potential. In the polar coordinates (r, θ) centred at the Sun, the dark matter trajectory can be expressed as

$$r = \frac{v_0^2 b^2}{GM_\odot} \frac{1}{1 + e\cos\theta}, \quad e = \sqrt{1 + b^2 \left(\frac{v_0^2}{GM_\odot}\right)^2} \tag{27}$$

where b is the impact factor and e is the eccentricity of the trajectory. The tangential velocity v_θ and radial velocity v_r of dark matter are, respectively

$$v_\theta = v_0 \frac{b}{r}, \quad v_r = \sqrt{v_0^2 - v_\theta^2 + \frac{2GM_\odot}{r}}, \quad v^2 = v_r^2 + v_\theta^2. \tag{28}$$

The dark matter velocity v_0 follows the Maxwellian distribution in the Galactic frame [79–81]:

$$f_G(v_0) = \frac{4}{\sqrt{\pi}} \frac{v_0^2}{v_p^3} \exp\left(-\frac{v_0^2}{v_p^2}\right), \tag{29}$$

and we have $\int_0^\infty dv_0 f_G(v_0) = 1$. v_p is the most probable speed, which is taken as the speed of local standard of rest, i.e., the circular speed about the Galactic centre at the solar position, $v_p \simeq v_\odot \simeq 220$ km/s. The distribution in Equation (29) should be truncated at $v_{\rm esp}$ which is the Galactic escape speed at the solar position, $v_{\rm esp} \simeq 544$ km/s. However, this modification is exponentially tiny as $\int_{v_{\rm esp}}^\infty dv_0 f_G(v_0) \approx 0.66\%$, which can be safely ignored. Next, we make a Galilean boost to obtain the velocity distribution in the rest frame of the Sun (e.g., [80]):

$$f(v_0) = \frac{1}{\sqrt{\pi}} \frac{v_0}{v_p v_\odot} \left\{ \exp\left[-\frac{(v_0 - v_\odot)^2}{v_p^2}\right] - \exp\left[-\frac{(v_0 + v_\odot)^2}{v_p^2}\right] \right\}. \tag{30}$$

Dark photons or axions in the dark matter wind can reach the resonant-conversion layer r_c if their impact parameters b are within

$$b_{\rm max} = r_c \frac{v(r_c)}{v_0} = r_c \sqrt{1 + \frac{2GM_\odot}{v_0^2 r_c}}. \tag{31}$$

Then, the total power of the converted photons per unit of solid angle flowing out of the sphere r_c is [67]

$$\frac{d\mathcal{P}_0}{d\Omega} = 2 \times \frac{1}{4\pi}\rho_{\rm DM} v_0 \cdot \int_0^{b_{\rm max}} db 2\pi b \cdot P_{X\to\gamma} = r_c^2 P_{X\to\gamma}(v_0)\rho_{\rm DM} v(r_c). \tag{32}$$

The prefactor 2 accounts for the fact that the dark matter particles entering and leaving the resonant sphere can both resonantly convert into photons with equal probability. The converted photons propagating inward will be totally reflected as the plasma frequency is larger in deeper regions. Then, with the Maxwellian velocity distribution (Equation (30)) taken into consideration, the emitted power (Equation (32)) is corrected as [78]

$$\frac{d\mathcal{P}}{d\Omega} = \int_0^\infty dv_0 f(v_0) \frac{d\mathcal{P}_0}{d\Omega}. \tag{33}$$

The converted photons will generate a spike-like feature superimposed on the normal solar radio spectrum. Such signals can be detected by radio telescopes, such as SKA and LOFAR, when they reach Earth. For Earth-based radio telescopes, the spectral flux density (in $\mathrm{W/m^2/Hz}$) received is thus [67,78]

$$S_{\rm sig} = \frac{1}{d^2}\frac{1}{\mathcal{B}}\frac{d\mathcal{P}}{d\Omega} \cdot P_{\rm sur} \cdot \beta[g(\theta)]. \tag{34}$$

The factor β represents the suppression on the final detected signal due to the scattering effect. It depends on the angular distribution $g(\theta)$ that requires a detailed ray-tracing numerical simulation [78]. If there is no scattering effect, then $\beta = 1$. $\mathcal{B}$ is the frequency bandwidth over which the signal distributes. We average the signal over the bandwidth and obtain the signal per unit of frequency as shown in Equation (34). $\mathcal{B}$ should be chosen as the larger one between the telescope resolution $\mathcal{B}_{\rm res}$ and the natural bandwidth $\mathcal{B}_{\rm DM}$. Due to the velocity dispersion of dark matter, the converted photons have a natural bandwidth of frequency [67,82]:

$$\mathcal{B}_{\rm DM} \simeq \frac{1}{2\pi} m_X v_p^2 \simeq 0.15\ \mathrm{kHz} \times \left(\frac{m_X}{10^{-6}\ \mathrm{eV}}\right). \tag{35}$$

On the other hand, we need to know the telescope's ability to detect weak signals. The minimal detectable spectral flux density of a telescope is [67,83]

$$S_{\rm min} = \frac{\mathrm{SEFD}}{\eta_s \sqrt{n_{\rm pos}\mathcal{B}t_{\rm obs}}}. \tag{36}$$

where η_s is the system efficiency of a telescope, which is 0.9 and 1 for SKA and LOFAR, respectively, [83,84]; $n_{\rm pol} = 2$ is the number of polarizations of photons; and $t_{\rm obs}$ is the observation time. SEFD is the system equivalent (spectral) flux density:

$$\mathrm{SEFD} = 2k_B \frac{T^{\rm sys} + T^{\rm nos}_\odot}{A_{\rm eff}}. \tag{37}$$

where $T^{\rm sys}$ is the system temperature of the radio telescope antenna; $T^{\rm nos}_\odot$ is the noise temperature induced on the antenna when pointing towards the Sun, which can be estimated as the black-body temperature of the quiet Sun [67]; and $A_{\rm eff}$ is the effective area of the radio telescope array such as SKA and LOFAR.

Then, taking the signal (Equation (34)) equal to the telescope detection ability (Equation (36)),

$$S_{\rm sig} = S_{\rm min}, \tag{38}$$

one can find the upper limit of the coupling $g_{a\gamma\gamma}$ for the axion case or ϵ for the dark photon case that can be detected by the telescope. Equation (38) reflects how large the

parameter space of dark photon/axion dark matter can be explored via observing solar radio emissions.

Ref. [67] used the SKA phase 1 (SKA1) and LOFAR as benchmark telescopes. To be specific, the following frequency ranges have been considered: the low-frequency band, SKA1-Low (50–350 MHz); two middle-frequency bands, SKA1-Mid B1 (350–1050 MHz) and B2 (950–1760 MHz); and two LOFAR frequency bands, (10–80 MHz) (low-band antenna) and (120–240 MHz) (high-band antenna). Note that LOFAR does not operate in the gap frequency range (80–120 MHz) due to the contamination from the human-made frequency-modulation (FM) broadcast band that spans over ∼(87–108 MHz) [47,85].

The effective area $A_{\rm eff}$ for SKA1 is about 10^4–10^5 m^2, while it is about 10^3 m^2 for LOFAR. The antenna system temperatures $T^{\rm sys}$ are also given in [67] based on the data of [47,83], ranging from ∼10 to 10^4 K for the five frequency bands. Lastly, the telescope resolution $\mathcal{B}_{\rm res}$ for SKA1-Low, SKA1-Mid and LOFAR are, 1, 3.5 and 197 kHz, respectively. All of them are larger than the natural bandwidth of dark matter (Equation (35)) for the radio frequency bands we are interested in. Therefore, one should choose $\mathcal{B} = \mathcal{B}_{\rm res}$ when computing the received signal (Equation (34)).

With the above properties of the radio telescopes known, the sensitivity for the dark photon case based on Equation (38) is plotted in Figure 2. The observation time is assumed to be 1 and 100 h, respectively. As shown in the plot, the sensitivity of the kinetic mixing parameter ϵ based on the SKA and LOFAR radio telescopes could be several orders of magnitude better than the existing constraints from the cosmic microwave background (CMB) [8,86] and the cavity experiment WISPDMX [87].

The sensitivity obtained in Figure 2 can be translated to the axion case via the relation in Equation (21), and the result is plotted in Figure 3. As shown in [88], the magnetic field strength is about 1–4 Gauss in the solar corona at 1.05–1.35 $R_\odot$ from the Sun centre. To be conservative, we take the transverse magnetic field $|\boldsymbol{B}_T| = 1$ Gauss in Equation (21). As we can see from Figure 3, our projected sensitivities are better than the light-shining-through-a-wall experiments (LSW, including CROWS, ALPS, and OSQAR [89–91]). Furthermore, they are better than the constraint from the CAST experiment in part of the SKA1 frequency range. However, in most of the relevant frequency range, they cannot exceed the constraints from multiple astrophysical searches in various environments [57,92–98] (shown as a combined constraint in Figure 3). The performance of sensitivity in the axion case is not as good as that in the dark photon case. This is because the solar magnetic field is relatively low which suppresses the axion–photon conversion rate as we can see from Equation (21).

Figures 2 and 3 are based on the simplified scenario of the propagation process of the converted photons that took $P_{\rm sur}$ in Equation (26) and assumed $\beta = 1$ in Equation (34). Instead, Ref. [78] numerically simulated the radio photon propagation based on the Monte Carlo ray-tracing method. Furthermore, the Maxwellian velocity distribution has been considered in computing the emitted power (Equation (33)), although this effect does not make much difference. Furthermore, Ref. [78] analysed real data of LOFAR (three samples of 17 min observations at different dates). Finally, Ref. [78] obtained a constraint of $\epsilon \sim 10^{-13}$ about one to two orders of magnitude better than the CMB constraint [8,86] in the frequency range 30–80 MHz. This constraint is weaker than the projections in Figure 2, mainly because the angular distribution in Equation (34) of converted photons is based on the numerical simulation. A similar constraint on the axion–photon coupling strength $g_{a\gamma\gamma} \sim 10^{-9}$ GeV^{-1} has been obtained in the same frequency range [78], which is about one to two orders of magnitude better than the existing constraints from the LSW experiments [89–91], but does not exceed the constraints from the CAST experiment [99] and multiple astrophysical bounds [57,92–98].

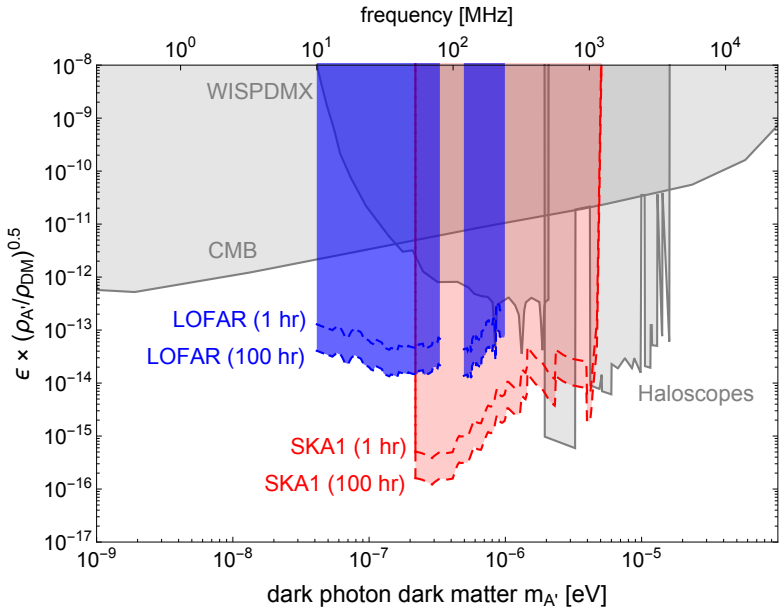

Figure 2. The projected sensitivity of the parameter space of the dark photon dark matter based on the radio telescopes SKA phase 1 and LOFAR, with the observation time assumed to be 1 and 100 h, respectively. The plot also shows the existing constraints from CMB [8,86], the cavity experiment WISPDMX [87], and the multiple haloscope-type experiments [8,100–104]. Figure adapted from [67].

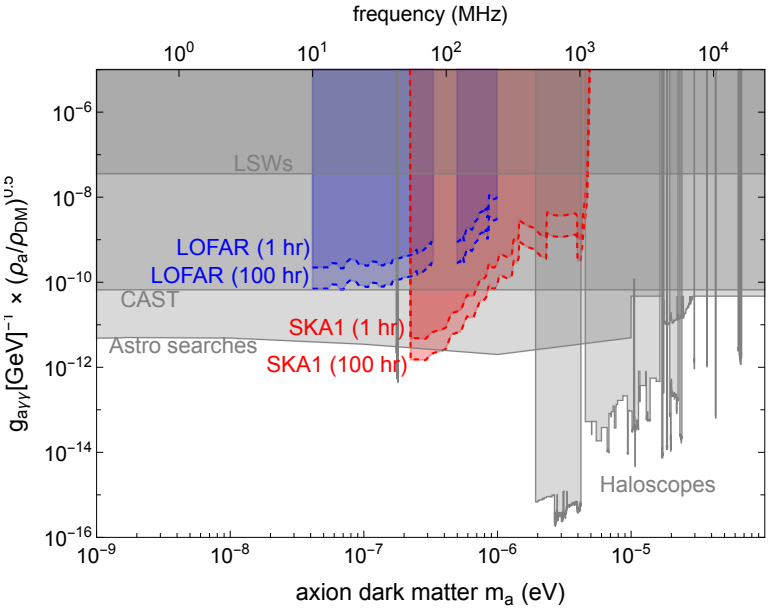

Figure 3. The projected sensitivity of the parameter space of the axion photon dark matter based on the radio telescopes SKA phase 1 and LOFAR, with the observation time assumed to be 1 and 100 h, respectively. The results are translated from Figure 2 via the relation in Equation (21) with $|\boldsymbol{B}_T|$ taken as 1 Gauss [88]. Together we show the existing constraints, which can be classified into four categories: the astrophysical searches for axions in various environments, including white dwarfs, neutron stars and pulsars, quasars and blazars, the radio galaxy NGC 1275, globular clusters, etc. [57,92–98]; various haloscope experiments aiming to detect axions in the galactic dark matter halo [100,102,104–125]; the helioscope, CAST, aiming to detect axions emitted by the Sun; and light-shining-through-a-wall (LSW) experiments including CROWS, ALPS, and OSQAR [89–91]. The existing constraints are also nicely summarized in [126].

In addition to the terrestrial facilities such as SKA and LOFAR discussed above, space radio probes are also powerful tools for searching for ultralight dark matter signals from resonant conversion. The STEREO observatory [49,127] consists of two nearly identical satellites, observing the Sun in the 1 AU orbit. It carries a low-frequency radio receiver operating in the frequency range 2.6–150 kHz and a higher-frequency receiver operating in the frequency range 125–16 MHz. Furthermore, the Parker solar probe [50,69] provides new opportunities for observing the conversion signal with the perihelion reaching $\sim 10 R_\odot$ from the Sun's centre. In fact, the Parker satellite is the first spacecraft that can fly into the solar corona. The best advantage for us is that the Parker satellite can measure in situ the resonant-conversion events in the solar-wind plasma as shown in Figure 1b, thanks to its motion between the Sun and 1 AU. The Parker satellite carries a low-frequency radio receiver operating in the frequency range 10–1.7 MHz and a higher-frequency radio receiver operating in the frequency range 1.3–19.2 MHz. We expect that the Parker satellite has a strong performance in searching for resonant-conversion signals in these frequency ranges. The analysis of space probes such as the Paker solar probe and STEREO to search for ultralight dark matter is currently in progress by the authors of this review.

6. Summary

Solar plasma is an ideal place for detecting ultralight axions or dark photons. When axion dark matter or dark photon dark matter particles cross the solar corona or solar wind, they can resonantly convert into standard model photons when their mass equals the plasma frequency. The plasma frequency of the solar corona and solar wind spans from 1 GHz to 0.1 MHz for the distance extending up to 1 AU. Therefore, searching for radio signals converted from ultralight axions or dark photons in the plasma provides a complementary method to other haloscope studies, to detect these dark matter particles in the mass range $\sim 10^{-6}$–10^{-10} eV and set stringent constraints on the parameter space of these dark matter models. Based on this mechanism, radio telescopes, such as LOFAR and SKA, perform well in searching for ultralight dark matter, especially for the dark photon case. Future projected SKA and upgraded FAST are expected to obtain solar radio data with much higher precision. In addition to the terrestrial telescopes, we can use space solar probes, such as STEREO and Parker, to search for the ultralight dark matter. We conclude that searching for resonant-conversion radio signals from solar plasma is an efficient method, which is competitive and complementary compared to other direct detection experiments [8,87,89–91,99–104] aiming for the ultralight dark matter.

Funding: The work of H.A. is supported in part by the National Key R&D Program of China under Grant No. 2021YFC2203100 and 2017YFA0402204, the NSFC under Grant No. 11975134, and the Tsinghua University Initiative Scientific Research Program. The work of SG is supported by NSFC under Grant No. 12247147, the International Postdoctoral Exchange Fellowship Program, and the Boya Postdoctoral Fellowship of Peking University. The work of J.L. is supported by NSFC under Grant No. 12075005, 12235001.

Data Availability Statement: The data presented in this work is available upon request from the corresponding author.

Conflicts of Interest: The authors declare no conflict of interest.

References

1. Akerib, D.S.; Alsum, S.; Araújo, H.M.; Bai, X.; Bailey, A.J.; Balajthy, J.; Beltrame, P.; Bernard, E.P.; Bernstein, A.; Biesiadzinski, T.P.; et al. Results from a search for dark matter in the complete LUX exposure. *Phys. Rev. Lett.* **2017**, *118*, 021303. [CrossRef] [PubMed]
2. Aprile, E.; Aprile, E.; Aalbers, J.; Agostini, F.; Alfonsi, M.; Althueser, L.; Amaro, F.D.; Anthony, M.; Arneodo, F.; Baudis, L.; et al. Dark Matter Search Results from a One Ton-Year Exposure of XENON1T. *Phys. Rev. Lett.* **2018**, *121*, 111302. [CrossRef] [PubMed]
3. Meng, Y.; Wang, Z.; Tao, Y.; Abdukerim, A.; Bo, Z.; Chen, W.; Chen, X.; Chen, Y.; Cheng, C.; Cheng, Y.; et al. Dark Matter Search Results from the PandaX-4T Commissioning Run. *Phys. Rev. Lett.* **2021**, *127*, 261802. [CrossRef]
4. Ipser, J.; Sikivie, P. Can Galactic Halos Made of Axions? *Phys. Rev. Lett.* **1983**, *50*, 925. [CrossRef]
5. Svrcek, P.; Witten, E. Axions In String Theory. *JHEP* **2006**, *6*, 51. [CrossRef]

6. Redondo, J.; Postma, M. Massive hidden photons as lukewarm dark matter. *JCAP* **2009**, *2*, 5. [CrossRef]
7. Nelson, A.E.; Scholtz, J. Dark Light, Dark Matter and the Misalignment Mechanism. *Phys. Rev.* **2011**, *D84*, 103501. [CrossRef]
8. Arias, P.; Cadamuro, D.; Goodsell, M.; Jaeckel, J.; Redondo, J.; Ringwald, A. WISPy Cold Dark Matter. *JCAP* **2012**, *1206*, 13. [CrossRef]
9. Graham, P.W.; Mardon, J.; Rajendran, S. Vector Dark Matter from Inflationary Fluctuations. *Phys. Rev.* **2016**, *D93*, 103520. [CrossRef]
10. Peccei, R.D.; Quinn, H.R. CP Conservation in the Presence of Instantons. *Phys. Rev. Lett.* **1977**, *38*, 1440–1443.
11. Peccei, R.D.; Quinn, H.R. Constraints Imposed by CP Conservation in the Presence of Instantons. *Phys. Rev. D* **1977**, *16*, 1791–1797. [CrossRef]
12. Weinberg, S. A New Light Boson? *Phys. Rev. Lett.* **1978**, *40*, 223–226. [CrossRef]
13. Wilczek, F. Problem of Strong *P* and *T* Invariance in the Presence of Instantons. *Phys. Rev. Lett.* **1978**, *40*, 279–282. [CrossRef]
14. Preskill, J.; Wise, M.B.; Wilczek, F. Cosmology of the Invisible Axion. *Phys. Lett.* **1983**, *B120*, 127–132. [CrossRef]
15. Abbott, L.F.; Sikivie, P. A Cosmological Bound on the Invisible Axion. *Phys. Lett.* **1983**, *B120*, 133–136. [CrossRef]
16. Dine, M.; Fischler, W. The Not So Harmless Axion. *Phys. Lett.* **1983**, *B120*, 137–141.
17. Vilenkin, A.; Everett, A.E. Cosmic strings and domain walls in models with Goldstone and pseudo-Goldstone bosons. *Phys. Rev. Lett.* **1982**, *48*, 1867. [CrossRef]
18. Sikivie, P. Axions, domain walls, and the early universe. *Phys. Rev. Lett.* **1982**, *48*, 1156. [CrossRef]
19. Holdom, B. Two U(1)'s and Epsilon Charge Shifts. *Phys. Lett.* **1986**, *166B*, 196–198. [CrossRef]
20. Dienes, K.R.; Kolda, C.F.; March-Russell, J. Kinetic mixing and the supersymmetric gauge hierarchy. *Nucl. Phys. B* **1997**, *492*, 104–118. [CrossRef]
21. Abel, S.A.; Schofield, B.W. Brane anti-brane kinetic mixing, millicharged particles and SUSY breaking. *Nucl. Phys. B* **2004**, *685*, 150–170.
22. Abel, S.A.; Goodsell, M.D.; Jaeckel, J.; Khoze, V.V.; Ringwald, A. Kinetic Mixing of the Photon with Hidden U(1)s in String Phenomenology. *JHEP* **2008**, *7*, 124. [CrossRef]
23. Abel, S.A.; Jaeckel, J.; Khoze, V.V.; Ringwald, A. Illuminating the Hidden Sector of String Theory by Shining Light through a Magnetic Field. *Phys. Lett. B* **2008**, *666*, 66–70.
24. Goodsell, M.; Jaeckel, J.; Redondo, J.; Ringwald, A. Naturally Light Hidden Photons in LARGE Volume String Compactifications. *JHEP* **2009**, *11*, 27. [CrossRef]
25. Co, R.T.; Pierce, A.; Zhang, Z.; Zhao, Y. Dark Photon Dark Matter Produced by Axion Oscillations. *Phys. Rev. D* **2019**, *99*, 075002. [CrossRef]
26. Dror, J.A.; Harigaya, K.; Narayan, V. Parametric Resonance Production of Ultralight Vector Dark Matter. *Phys. Rev. D* **2019**, *99*, 035036. [CrossRef]
27. Bastero-Gil, M.; Santiago, J.; Ubaldi, L.; Vega-Morales, R. Vector dark matter production at the end of inflation. *J. Cosmol. Astropart. Phys.* **2019**, *4*, 15. [CrossRef]
28. Agrawal, P.; Kitajima, N.; Reece, M.; Sekiguchi, T.; Takahashi, F. Relic Abundance of Dark Photon Dark Matter. *Phys. Lett. B* **2020**, *801*, 135136. [CrossRef]
29. Co, R.T.; Harigaya, K.; Pierce, A. Gravitational waves and dark photon dark matter from axion rotations. *JHEP* **2021**, *12*, 99. [CrossRef]
30. Nakayama, K.; Yin, W. Hidden photon and axion dark matter from symmetry breaking. *JHEP* **2021**, *10*, 26. [CrossRef]
31. Ema, Y.; Nakayama, K.; Tang, Y. Production of Purely Gravitational Dark Matter: The Case of Fermion and Vector Boson. *JHEP* **2019**, *7*, 60. [CrossRef]
32. Kolb, E.W.; Long, A.J. Completely dark photons from gravitational particle production during the inflationary era. *JHEP* **2021**, *3*, 283.
33. Salehian, B.; Gorji, M.A.; Firouzjahi, H.; Mukohyama, S. Vector dark matter production from inflation with symmetry breaking. *Phys. Rev. D* **2021**, *103*, 063526. [CrossRef]
34. Ahmed, A.; Grzadkowski, B.; Socha, A. Gravitational production of vector dark matter. *JHEP* **2020**, *8*, 59. [CrossRef]
35. Nakai, Y.; Namba, R.; Wang, Z. Light Dark Photon Dark Matter from Inflation. *JHEP* **2020**, *12*, 170. [CrossRef]
36. Nakayama, K.; Tang, Y. Gravitational Production of Hidden Photon Dark Matter in Light of the XENON1T Excess. *Phys. Lett. B* **2020**, *811*, 135977, [CrossRef]
37. Firouzjahi, H.; Gorji, M.A.; Mukohyama, S.; Salehian, B. Dark photon dark matter from charged inflaton. *JHEP* **2021**, *6*, 50, [CrossRef]
38. Bastero-Gil, M.; Santiago, J.; Ubaldi, L.; Vega-Morales, R. Dark photon dark matter from a rolling inflaton. *JCAP* **2022**, *2*, 15. [CrossRef]
39. Firouzjahi, H.; Gorji, M.A.; Mukohyama, S.; Talebian, A. Dark matter from entropy perturbations in curved field space. *Phys. Rev. D* **2022**, *105*, 43501.
40. Sato, T.; Takahashi, F.; Yamada, M. Gravitational production of dark photon dark matter with mass generated by the Higgs mechanism. *J. Cosmol. Astropart. Phys.* **2022**, *8*, 22. [CrossRef]
41. Alonso-Álvarez, G.; Hugle, T.; Jaeckel, J. Misalignment & Co.: (Pseudo-)scalar and vector dark matter with curvature couplings. *J. Cosmol. Astropart. Phys.* **2020**, *2*, 14.

42. Nakayama, K. Vector Coherent Oscillation Dark Matter. *JCAP* **2019**, *1910*, 19. [CrossRef]
43. Nakayama, K. Constraint on Vector Coherent Oscillation Dark Matter with Kinetic Function. *JCAP* **2020**, *8*, 33. [CrossRef]
44. Long, A.J.; Wang, L.T. Dark Photon Dark Matter from a Network of Cosmic Strings. *Phys. Rev. D* **2019**, *99*, 063529. [CrossRef]
45. de Salas, P.F.; Malhan, K.; Freese, K.; Hattori, K.; Valluri, M. On the estimation of the Local Dark Matter Density using the rotation curve of the Milky Way. *JCAP* **2019**, *10*, 37.
46. de Salas, P.F.; Widmark, A. Dark matter local density determination: Recent observations and future prospects. *Rept. Prog. Phys.* **2021**, *84*, 104901.
47. van Haarlem, M.P.; Wise, M.W.; Gunst, A.W.; Heald, G.; McKean, J.P.; Hessels, J.W.; de Bruyn, A.G.; Nijboer, R.; Swinbank, J.; Fallows, R.; et al. LOFAR: The LOw-Frequency ARray. *Astron. Astrophys.* **2013**, *556*, A2.
48. Dewdney, P.E.; Hall, P.J.; Schilizzi, R.T.; Lazio, T.J.L. The square kilometre array. *Proc. IEEE* **2009**, *97*, 1482–1496. [CrossRef]
49. Kaiser, M.L.; Kucera, T.; Davila, J.; St Cyr, O.; Guhathakurta, M.; Christian, E. The STEREO mission: An introduction. *Space Sci. Rev.* **2008**, *136*, 5–16. [CrossRef]
50. Pulupa, M.; Bale, S.D.; Bonnell, J.W.; Bowen, T.A.; Carruth, N.; Goetz, K.; Gordon, D.; Harvey, P.R.; Maksimovic, M.; Martínez-Oliveros, J.C.; et al. The solar probe plus radio frequency spectrometer: Measurement requirements, analog design, and digital signal processing. *J. Geophys. Res. Space Phys.* **2017**, *122*, 2836–2854. [CrossRef]
51. Pshirkov, M.S.; Popov, S.B. Conversion of Dark matter axions to photons in magnetospheres of neutron stars. *J. Exp. Theor. Phys.* **2009**, *108*, 384–388.
52. Huang, F.P.; Kadota, K.; Sekiguchi, T.; Tashiro, H. Radio telescope search for the resonant conversion of cold dark matter axions from the magnetized astrophysical sources. *Phys. Rev. D* **2018**, *97*, 123001. [CrossRef]
53. Hook, A.; Kahn, Y.; Safdi, B.R.; Sun, Z. Radio Signals from Axion Dark Matter Conversion in Neutron Star Magnetospheres. *Phys. Rev. Lett.* **2018**, *121*, 241102. [CrossRef]
54. Hardy, E.; Song, N. Listening for Dark Photon Radio from the Galactic Centre. *arXiv* **2022**, arXiv:2212.09756.
55. Wang, J.W.; Bi, X.J.; Yao, R.M.; Yin, P.F. Exploring axion dark matter through radio signals from magnetic white dwarf stars. *Phys. Rev. D* **2021**, *103*, 115021. [CrossRef]
56. Dessert, C.; Long, A.J.; Safdi, B.R. X-ray Signatures of Axion Conversion in Magnetic White Dwarf Stars. *Phys. Rev. Lett.* **2019**, *123*, 061104. [CrossRef] [PubMed]
57. Dessert, C.; Dunsky, D.; Safdi, B.R. Upper limit on the axion-photon coupling from magnetic white dwarf polarization. *Phys. Rev. D* **2022**, *105*, 103034. [CrossRef]
58. Mondal, S.; Oberoi, D.; Mohan, A. First Radio Evidence for Impulsive Heating Contribution to the Quiet Solar Corona. *Astrophys. J. Lett.* **2020**, *895*, L39.
59. Zhitnitsky, A.R. 'Nonbaryonic' dark matter as baryonic color superconductor. *JCAP* **2003**, *10*, 10.
60. Liang, X.; Zhitnitsky, A. Axion field and the quark nugget's formation at the QCD phase transition. *Phys. Rev. D* **2016**, *94*, 083502. [CrossRef]
61. Ge, S.; Liang, X.; Zhitnitsky, A. Cosmological axion and a quark nugget dark matter model. *Phys. Rev. D* **2018**, *97*, 043008. [CrossRef]
62. Ge, S.; Liang, X.; Zhitnitsky, A. Cosmological CP odd axion field as the coherent Berry's phase of the Universe. *Phys. Rev. D* **2017**, *96*, 063514. [CrossRef]
63. Ge, S.; Lawson, K.; Zhitnitsky, A. Axion quark nugget dark matter model: Size distribution and survival pattern. *Phys. Rev. D* **2019**, *99*, 116017. [CrossRef]
64. Zhitnitsky, A. Solar Extreme UV radiation and quark nugget dark matter model. *JCAP* **2017**, *10*, 50.
65. Raza, N.; van Waerbeke, L.; Zhitnitsky, A. Solar corona heating by axion quark nugget dark matter. *Phys. Rev. D* **2018**, *98*, 103527.
66. Ge, S.; Siddiqui, M.S.R.; Van Waerbeke, L.; Zhitnitsky, A. Impulsive radio events in quiet solar corona and axion quark nugget dark matter. *Phys. Rev. D* **2020**, *102*, 123021.
67. An, H.; Huang, F.P.; Liu, J.; Xue, W. Radio-frequency Dark Photon Dark Matter across the Sun. *Phys. Rev. Lett.* **2021**, *126*, 181102. [CrossRef]
68. De La Luz, V.; Lara, A.; Mendoza, E.; Shimojo, M. 3D Simulations of the Quiet Sun Radio Emission at Millimeter and Submillimeter Wavelengths. *Geofis. Int.* **2008**, *47*, 197–203. [CrossRef]
69. Moncuquet, M.; Meyer-Vernet, N.; Issautier, K.; Pulupa, M.; Bonnell, J.W.; Bale, S.D.; de Wit, T.D.; Goetz, K.; Griton, L.; Harvey, P.R.; et al. First In Situ Measurements of Electron Density and Temperature from Quasi-thermal Noise Spectroscopy with Parker Solar Probe /FIELDS. *Astrophys. J. Suppl. Ser.* **2020**, *246*, 44. [CrossRef]
70. Leblanc, Y.; Dulk, G.A.; Bougeret, J.L. Tracing the Electron Density from the Corona to 1 au. *Sol. Phys.* **1998**, *183*, 165–180. [CrossRef]
71. Raffelt, G.; Stodolsky, L. Mixing of the Photon with Low Mass Particles. *Phys. Rev.* **1988**, *D37*, 1237. [CrossRef]
72. Redondo, J. Helioscope Bounds on Hidden Sector Photons. *JCAP* **2008**, *807*, 8. [CrossRef]
73. Kontar, E.P.; Chen, X.; Chrysaphi, N.; Jeffrey, N.L.S.; Emslie, A.G.; Krupar, V.; Maksimovic, M.; Gordovskyy, M.; Browning, P.K. Anisotropic Radio-wave Scattering and the Interpretation of Solar Radio Emission Observations. *Astrophys. J.* **2019**, *884*, 122. [CrossRef]
74. Thejappa, G.; MacDowall, R.J.; Kaiser, M.L. Monte Carlo Simulation of Directivity of Interplanetary Radio Bursts. *Astrophys. J.* **2007**, *671*, 894–906. [CrossRef]

75. Bian, N.H.; Emslie, A.G.; Kontar, E.P. A Fokker–Planck Framework for Studying the Diffusion of Radio Burst Waves in the Solar Corona. *Astrophys. J.* **2019**, *873*, 33. [CrossRef]
76. Acharya, S.K.; Chluba, J.; Sarkar, A. Comparison of numerical methods for computing the repeated Compton scattering of photons in isotropic media. *Mon. Not. R. Astron. Soc.* **2021**, *507*, 2052–2072. [CrossRef]
77. Cooper, G. Compton Fokker–Planck equation for hot plasmas. *Phys. Rev. D* **1971**, *3*, 2312. [CrossRef]
78. An, H.; Chen, X.; Ge, S.; Liu, J.; Luo, Y. Searching for Ultralight Dark Matter Conversion in Solar Corona using LOFAR Data. *arXiv* **2023**, arXiv:2301.03622.
79. Drukier, A.K.; Freese, K.; Spergel, D.N. Detecting Cold Dark Matter Candidates. *Phys. Rev. D* **1986**, *33*, 3495–3508. [CrossRef] [PubMed]
80. Choi, K.; Rott, C.; Itow, Y. Impact of the dark matter velocity distribution on capture rates in the Sun. *JCAP* **2014**, *5*, 49.
81. Evans, N.W.; O'Hare, C.A.J.; McCabe, C. Refinement of the standard halo model for dark matter searches in light of the Gaia Sausage. *Phys. Rev. D* **2019**, *99*, 023012,
82. An, H.; Ge, S.; Guo, W.Q.; Huang, X.; Liu, J.; Lu, Z. Direct detection of dark photon dark matter using radio telescopes. *arXiv* **2022**, arXiv:2207.05767.
83. SKA-Collaboration. SKA1 System Baseline Design. 2013. Document number: SKA-TEL-SKO-DD-001. Available online: https://www.skatelescope.org/wp-content/uploads/2014/11/SKA-TEL-SKO-0000002-AG-BD-DD-Rev01-SKA1_System_Baseline_Design.pdf (accessed on 2 March 2023).
84. Nijboer, R.J.; Pandey-Pommier, M.; de Bruyn, A.G. LOFAR imaging capabilities and system sensitivity. *arXiv* **2013**, arXiv:1308.4267.
85. de Vos, M.; Gunst, A.W.; Nijboer, R. The LOFAR Telescope: System Architecture and Signal Processing. *IEEE Proc.* **2009**, *97*, 1431–1437. [CrossRef]
86. McDermott, S.D.; Witte, S.J. Cosmological evolution of light dark photon dark matter. *Phys. Rev.* **2020**, *D101*, 063030. [CrossRef]
87. Hoang Nguyen, L.; Lobanov, A.; Horns, D. First results from the WISPDMX radio frequency cavity searches for hidden photon dark matter. *JCAP* **2019**, *1910*, 14.
88. Yang, Z.; Bethge, C.; Tian, H.; Tomczyk, S.; Morton, R.; Del Zanna, G.; McIntosh, S.W.; Karak, B.B.; Gibson, S.; Samanta, T.; et al. Global maps of the magnetic field in the solar corona. *Science* **2020**, *369*, 694–697. [CrossRef]
89. Betz, M.; Caspers, F.; Gasior, M.; Thumm, M.; Rieger, S.W. First results of the CERN Resonant Weakly Interacting sub-eV Particle Search (CROWS). *Phys. Rev. D* **2013**, *88*, 075014.
90. Ehret, K.; Frede, M.; Ghazaryan, S.; Hildebrandt, M.; Knabbe, E.A.; Kracht, D.; Lindner, A.; List, J.; Meier, T.; Meyer, N.; et al. New ALPS Results on Hidden-Sector Lightweights. *Phys. Lett. B* **2010**, *689*, 149–155.
91. Ballou, R.; Deferne, G.; Finger, M., Jr.; Finger, M.; Flekova, L.; Hosek, J.; Kunc, S.; Macuchova, K.; Meissner, K.A.; Pugnat, P.; et al. New exclusion limits on scalar and pseudoscalar axionlike particles from light shining through a wall. *Phys. Rev. D* **2015**, *92*, 092002.
92. Ayala, A.; Domínguez, I.; Giannotti, M.; Mirizzi, A.; Straniero, O. Revisiting the bound on axion-photon coupling from Globular Clusters. *Phys. Rev. Lett.* **2014**, *113*, 191302.
93. Dolan, M.J.; Hiskens, F.J.; Volkas, R.R. Advancing globular cluster constraints on the axion-photon coupling. *JCAP* **2022**, *10*, 96. [CrossRef]
94. Noordhuis, D.; Prabhu, A.; Witte, S.J.; Chen, A.Y.; Cruz, F.; Weniger, C. Novel Constraints on Axions Produced in Pulsar Polar Cap Cascades. *arXiv* **2022**, arXiv:2209.09917.
95. Li, H.J.; Guo, J.G.; Bi, X.J.; Lin, S.J.; Yin, P.F. Limits on axion-like particles from Mrk 421 with 4.5-year period observations by ARGO-YBJ and Fermi-LAT. *Phys. Rev. D* **2021**, *103*, 083003.
96. Li, H.J.; Bi, X.J.; Yin, P.F. Searching for axion-like particles with the blazar observations of MAGIC and Fermi-LAT. *Chin. Phys. C* **2022**, *46*, 085105.
97. Davies, J.; Meyer, M.; Cotter, G. Constraints on axionlike particles from a combined analysis of three flaring *Fermi* flat-spectrum radio quasars. *arXiv* **2022**, arXiv:2211.03414.
98. Ajello, M.; Albert, A.; Anderson, B.; Baldini, L.; Barbiellini, G.; Bastieri, D.; Bellazzini, R.; Bissaldi, E.; Blandford, R.D.; Bloom, E.D.; et al. Search for Spectral Irregularities due to Photon–Axionlike-Particle Oscillations with the Fermi Large Area Telescope. *Phys. Rev. Lett.* **2016**, *116*, 161101.
99. Anastassopoulos, V.; Aune, S.; Barth, K.; Belov, A.; Cantatore, G.; Carmona, J.M.; Castel, J.F.; Cetin, S.A.; Christensen, F.; Collar, J.I.; et al. New CAST Limit on the Axion-Photon Interaction. *Nat. Phys.* **2017**, *13*, 584–590. [CrossRef]
100. De Panfilis, S.; Melissinos, A.C.; Moskowitz, B.E.; Rogers, J.T.; Semertzidis, Y.K.; Wuensch, W.; Halama, H.J.; Prodell, A.G.; Fowler, W.B.; Nezrick, F.A. Limits on the Abundance and Coupling of Cosmic Axions at 4.5-Microev < m(a) < 5.0-Microev. *Phys. Rev. Lett.* **1987**, *59*, 839. [CrossRef]
101. Wuensch, W.; De Panfilis-Wuensch, S.; Semertzidis, Y.K.; Rogers, J.T.; Melissinos, A.C.; Halama, H.J.; Moskowitz, B.E.; Prodell, A.G.; Fowler, W.B.; Nezrick, F.A. Results of a Laboratory Search for Cosmic Axions and Other Weakly Coupled Light Particles. *Phys. Rev.* **1989**, *D40*, 3153. [CrossRef]
102. Hagmann, C.; Sikivie, P.; Sullivan, N.S.; Tanner, D.B. Results from a search for cosmic axions. *Phys. Rev.* **1990**, *D42*, 1297–1300. [CrossRef]

103. Asztalos, S.J.; Daw, E.; Peng, H.; Rosenberg, L.J.; Hagmann, C.; Kinion, D.; Stoeffl, W.; van Bibber, K.; Sikivie, P.; Sullivan, N.S.; et al. Large scale microwave cavity search for dark matter axions. *Phys. Rev.* **2001**, *D64*, 092003. [CrossRef]
104. Asztalos, S.J.; Carosi, G.; Hagmann, C.; Kinion, D.; Van Bibber, K.; Hotz, M.; Rosenberg, L.J.; Rybka, G.; Hoskins, J.; Hwang, J.; et al. A SQUID-based microwave cavity search for dark-matter axions. *Phys. Rev. Lett.* **2010**, *104*, 041301.
105. Du, N.; Force, N.; Khatiwada, R.; Lentz, E.; Ottens, R.; Rosenberg, L.J.; Rybka, G.; Carosi, G.; Woollett, N.; Bowring, D.; et al. A Search for Invisible Axion Dark Matter with the Axion Dark Matter Experiment. *Phys. Rev. Lett.* **2018**, *120*, 151301.
106. Navarro, J.F.; Frenk, C.S.; White, S.D.M. A Universal Density Profile from Hierarchical Clustering. *Astrophys. J.* **1997**, *490*, 493. [CrossRef]
107. Braine, T.; Cervantes, R.; Crisosto, N.; Du, N.; Kimes, S.; Rosenberg, L.J.; Rybka, G.; Yang, J.; Bowring, D.; Chou, A.S.; et al. Extended Search for the Invisible Axion with the Axion Dark Matter Experiment. *Phys. Rev. Lett.* **2020**, *124*, 101303.
108. Boutan, C.; Jones, M.; LaRoque, B.H.; Oblath, N.S.; Cervantes, R.; Du, N.; Force, N.; Kimes, S.; Ottens, R.; Rosenberg, L.J.; et al. Piezoelectrically Tuned Multimode Cavity Search for Axion Dark Matter. *Phys. Rev. Lett.* **2018**, *121*, 261302.
109. Zhong, L.; Al Kenany, S.; Backes, K.M.; Brubaker, B.M.; Cahn, S.B.; Carosi, G.; Gurevich, Y.V.; Kindel, W.F.; Lamoreaux, S.K.; Lehnert, K.W.; et al. Results from phase 1 of the HAYSTAC microwave cavity axion experiment. *Phys. Rev. D* **2018**, *97*, 092001.
110. Backes, K.M.; Palken, D.A.; Kenany, S.A.; Brubaker, B.M.; Cahn, S.B.; Droster, A.; Hilton, G.C.; Ghosh, S.; Jackson, H.; Lamoreaux, S.K.; et al. A quantum-enhanced search for dark matter axions. *Nature* **2021**, *590*, 238–242.
111. Alesini, D.; Braggio, C.; Carugno, G.; Crescini, N.; D'Agostino, D.; Di Gioacchino, D.; Di Vora, R.; Falferi, P.; Gambardella, U.; Gatti, C.; et al. Search for invisible axion dark matter of mass $m_a = 43$ μeV with the QUAX–$a\gamma$ experiment. *Phys. Rev. D* **2021**, *103*, 102004.
112. Lee, S.; Ahn, S.; Choi, J.; Ko, B.R.; Semertzidis, Y.K. Axion Dark Matter Search around 6.7 μeV. *Phys. Rev. Lett.* **2020**, *124*, 101802.
113. Jeong, J.; Youn, S.; Bae, S.; Kim, J.; Seong, T.; Kim, J.E.; Semertzidis, Y.K. Search for Invisible Axion Dark Matter with a Multiple-Cell Haloscope. *Phys. Rev. Lett.* **2020**, *125*, 221302.
114. Kwon, O.; Lee, D.; Chung, W.; Ahn, D.; Byun, H.; Caspers, F.; Choi, H.; Choi, J.; Chong, Y.; Jeong, H.; et al. First Results from an Axion Haloscope at CAPP around 10.7 μeV. *Phys. Rev. Lett.* **2021**, *126*, 191802.
115. Bartram, C.; Braine, T.; Burns, E.; Cervantes, R.; Crisosto, N.; Du, N.; Korandla, H.; Leum, G.; Mohapatra, P.; Nitta, T.; et al. Search for Invisible Axion Dark Matter in the 3.3–4.2 μeV Mass Range. *Phys. Rev. Lett.* **2021**, *127*, 261803.
116. Crisosto, N.; Sikivie, P.; Sullivan, N.S.; Tanner, D.B.; Yang, J.; Rybka, G. ADMX SLIC: Results from a Superconducting *LC* Circuit Investigating Cold Axions. *Phys. Rev. Lett.* **2020**, *124*, 241101.
117. Lee, Y.; Yang, B.; Yoon, H.; Ahn, M.; Park, H.; Min, B.; Kim, D.; Yoo, J. Searching for Invisible Axion Dark Matter with an 18 T Magnet Haloscope. *Phys. Rev. Lett.* **2022**, *128*, 241805.
118. Kim, J.; Kwon, O.; Kutlu, C.; Chung, W.; Matlashov, A.; Uchaikin, S.; van Loo, A.F.; Nakamura, Y.; Oh, S.; Byun, H.; et al. Near-Quantum-Noise Axion Dark Matter Search at CAPP around 9.5 μeV. *arXiv* **2022**, arXiv:2207.13597.
119. Yi, A.K.; Ahn, S.; Kutlu, Ç.; Kim, J.; Ko, B.R.; Ivanov, B.I.; Byun, H.; van Loo, A.F.; Park, S.; Jeong, J.; et al. Axion Dark Matter Search around 4.55 μeV with Dine-Fischler-Srednicki-Zhitnitskii Sensitivity. *Phys. Rev. Lett.* **2022**, *130*, 071002. [CrossRef]
120. Adair, C.M.; Altenmüller, K.; Anastassopoulos, V.; Arguedas Cuendis, S.; Baier, J.; Barth, K.; Belov, A.; Bozicevic, D.; Bräuninger, H.; Cantatore, G.; et al. Search for Dark Matter Axions with CAST-CAPP. *Nature Commun.* **2022**, *13*, 6180. [CrossRef]
121. Jewell, M.J.; Leder, A.F.; Backes, K.M.; Bai, X.; van Bibber, K.; Brubaker, B.M.; Cahn, S.B.; Droster, A.; Esmat, M.H.; Ghosh, S.; et al. New Results from HAYSTAC's Phase II Operation with a Squeezed State Receiver. *arXiv* **2023**, arXiv:2301.09721.
122. Quiskamp, A.P.; McAllister, B.T.; Altin, P.; Ivanov, E.N.; Goryachev, M.; Tobar, M.E. Direct search for dark matter axions excluding ALP cogenesis in the 63- to 67-μeV range with the ORGAN experiment. *Sci. Adv.* **2022**, *8*, abq3765.
123. Alesini, D.; Braggio, C.; Carugno, G.; Crescini, N.; D'Agostino, D.; Di Gioacchino, D.; Di Vora, R.; Falferi, P.; Gallo, S.; Gambardella, U.; et al. Galactic axions search with a superconducting resonant cavity. *Phys. Rev. D* **2019**, *99*, 101101. [CrossRef]
124. Alesini, D.; Babusci, D.; Braggio, C.; Carugno, G.; Crescini, N.; D'Agostino, D.; D'Elia, A.; Di Gioacchino, D.; Di Vora, R.; Falferi, P.; et al. Search for Galactic axions with a high-Q dielectric cavity. *Phys. Rev. D* **2022**, *106*, 052007. [CrossRef]
125. Chang, H.; Chang, J.Y.; Chang, Y.C.,; Chang, Y.H.; Chang, Y.H.; Chen, C.H.; Chen, C.F.; Chen, K.Y.; Chen, Y.F.; Chiang, W.Y.; et al. First Results from the Taiwan Axion Search Experiment with a Haloscope at 19.6 μeV. *Phys. Rev. Lett.* **2022**, *129*, 111802.
126. O'Hare, C. Cajohare/AxionLimits: AxionLimits. 2020. Available online: https://cajohare.github.io/AxionLimits/ (accessed on 2 March 2023). [CrossRef]
127. Zaslavsky, A.; Meyer-Vernet, N.; Hoang, S.; Maksimovic, M.; Bale, S.D. On the antenna calibration of space radio instruments using the galactic background: General formulas and application to STEREO/WAVES. *Radio Sci.* **2011**, *46*, 1–7. [CrossRef]